THE JOURNAL OF PHYSICAL CHEMISTRY C

Article

Cite This: J. Phys. Chem. C 2018, 122, 28797−28804

pubs.acs.org/JPCC

Crystal Morphology and Phase Transformation of $LiAlO_2$: Combined Experimental and First-Principles Studies

Su Jeong Heo,[†] Rohit Batra,[‡] Rampi Ramprasad,[‡] and Prabhakar Singh*[,†]

[†]Department of Materials Science and Engineering, University of Connecticut, Storrs, Connecticut 06269, United States

[‡]School of Materials Science and Engineering, Georgia Institute of Technology, Atlanta, Georgia 31332, United States

Supporting Information

ABSTRACT: Layered α-$LiAlO_2$ matrix often suffers from detrimental structural and morphological changes during its lifetime, especially under H_2-containing fuel inlet environments of molten carbonate fuel cell systems. However, the underlying mechanism of this phase and the morphological transformations has rarely been explored. In this study, transmission electron microscopy (TEM) techniques were used to determine the changes in structure and morphology of $LiAlO_2$ samples lifted by a focused ion beam. In accordance with X-ray diffraction analysis, TEM images show that under H-rich conditions the rhombohedral α-$LiAlO_2$ transforms to tetragonal γ-$LiAlO_2$ phase with the appearance of the (101)-terminated octahedral-shaped γ-$LiAlO_2$ crystallites. We further support, and plausibly rationalize, the observed transformations using density functional theory (DFT) calculation. The DFT computed surface energies of γ-$LiAlO_2$ reveal that the {101} surface becomes the lowest energy surface upon H-adsorption, thus leading to formation of observed octahedral geometry. Contrary to stabilization of γ-$LiAlO_2$ surfaces upon H passivation, DFT revealed H adsorption on α-$LiAlO_2$ surfaces to be energetically unfavorable. This contrasting behavior of α-$LiAlO_2$ and γ-$LiAlO_2$ under H-rich environments could be a potential driving force for the observed α-$LiAlO_2$ to γ-$LiAlO_2$ phase transformation.

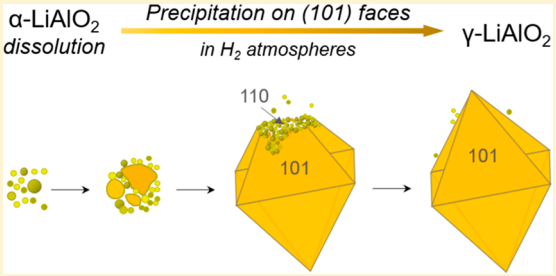

INTRODUCTION

$LiAlO_2$ is one of the most widely used electrode and electrolyte matrix materials for lithium-ion batteries and fuel cells because of its high energy and power densities, low cost, and physical and chemical stability at elevated temperature.[1,2] In the molten carbonate fuel cells (MCFC), $LiAlO_2$ plays an important role in retaining the liquid electrolyte and preventing gas crossover with its sufficiently stable fine-pore structure.[3,4] However, irreversible surface reconstruction of $LiAlO_2$ linked to particle coarsening and phase transition could occur during long-term exposure to the MCFC environment, which permanently deteriorates the cell performance.[5,6]

Extensive studies have been carried out to discover the origins of the degradation phenomena. For example, our previous studies[7] explained that $LiAlO_2$ could suffer from structural instability in reducing atmospheres containing excess hydrogen. Takizawa and Hagiwara[8] reported that the structure of $LiAlO_2$ became unstable at higher temperature and lower CO_2 partial pressures, leading to dissolution of $LiAlO_2$ into the electrolyte and consecutive structural reconstruction.[9] Furthermore, such dissolution of $LiAlO_2$ can induce the electrolyte decomposition, which causes the electrolyte depletion and thus results in degradation of cell performance.[10,11] However, studies detailing the atomic level structural (re)-arrangements/transformation and the underlying mechanisms have not been explored yet.

Bulk $LiAlO_2$ typically exists in two different allotropic forms: the rhombohedral α-$LiAlO_2$ and tetragonal γ-$LiAlO_2$. The α-$LiAlO_2$ crystallizes in the trigonal system ($R\bar{3}m$, space group 166) adopting the α-$NaFeO_2$ structure.[12] This structure can be interpreted as an ordered rock salt with consecutive alternating $[AlO_2]^-$ and Li^+ layers; the Al^{3+} and Li^+ ions are octahedrally coordinated in a cubic close-packed (ccp) O^{2-} lattice, resulting in a rhombohedral structure. Several materials such as $LiCoO_2$, $LiNiO_2$, and $NaMnO_2$ have the same crystal structure as α-$LiAlO_2$.[13−16] While past density functional theory (DFT) surface studies predicted $LiCoO_2$ and $LiNiO_2$ to adopt crystal shapes with (104), (003), and (012) surfaces, the (104) surface was found to be lowest in energy among the nonpolar surfaces, in agreement with the experimental findings.[17,18] Nonetheless, empirical and theoretical studies on α-$LiAlO_2$ remain absent.

The γ-$LiAlO_2$ structure consists of LiO_4 tetrahedra with Li^+ ions on corner-sharing octahedral positions and Li^+ ions on edge-sharing octahedral positions, the latter running parallel to the crystallographic b axis in the tetragonal symmetry with the space group $P4_12_12$ structure.[19] The γ-$LiAlO_2$ has been extensively explored as a substrate material for epitaxial growth of III−V semiconductors,[20] and as a tritium-breeder material in fusion reactors.[21,22] Despite widespread use of $LiAlO_2$, there are only a few theoretical studies on this material, with little understanding of its surface structure and crystal morphology.

Received: October 5, 2018
Revised: November 28, 2018
Published: December 3, 2018

DOI: 10.1021/acs.jpcc.8b09716
J. Phys. Chem. C 2018, 122, 28797−28804

To the best of our knowledge, comprehensive experimental and theoretical studies on $LiAlO_2$ particle morphologies and surface energetics are missing, although they are highly desired because of their many potential applications.

In this work, we first test the structural and morphological stability of α-$LiAlO_2$ under varying gas environments (reducing and oxidizing) expected during the operation of the fuel cells. We find that the rhombohedral α-phase transforms to the tetragonal γ-phase under H-rich environments, with the γ-$LiAlO_2$ phase appearing as microsized octahedral crystallites. Transmission electron microscopy (TEM) techniques were used to reveal the underlying surface arrangement and its structure, which are the key factors affecting the morphology of the sample. Furthermore, the empirical results are corroborated with simplified, yet informative, first-principles theoretical studies. Using DFT, we examine the surface energetics and morphological change of α- and γ-$LiAlO_2$ phases under H-free and H-rich conditions. The theoretical studies reveal that H adsorption is preferred on γ-$LiAlO_2$ surfaces, especially on (101), while its energetically unfavorable for α-$LiAlO_2$ surfaces. The DFT results not only provide support for observation of octahedral-shaped γ-$LiAlO_2$ particles but also hint at stabilization of γ-$LiAlO_2$ surfaces (relative to α-$LiAlO_2$) as the thermodynamic force driving empirically observed phase transformation. The combined empirical and theoretical study presented here provides a design of electrolyte matrix materials for more stable phase and particle morphologies in fuel cell environments as well as establishes a foundation for future mechanistic studies on $LiAlO_2$ surface instabilities.

EXPERIMENTAL AND THEORETICAL METHODS

Experimental Section. $LiAlO_2$ was prepared by solid-state synthesis method as reported in a previous study from our group.[23] The $LiAlO_2$ was immersed in a mixture of eutectic melt of composition 52:48 Li_2CO_3:Na_2CO_3 (mol %). The mixture of Li_2CO_3 (>99.0% pure, Sigma-Aldrich) and Na_2CO_3 (>99% pure, Sigma-Aldrich) were premelted at 500 °C. Both $LiAlO_2$ powder and Li/Na carbonate were put in a platinum crucible (99% pure, 30 mL, Sigma-Aldrich) and placed within a sealed closed one-end alumina reactor. The alumina reactor was subsequently heated to 650 °C at 3 °C/min. The immersion tests were conducted at 650 °C under controlled atmospheres (100 cm^3/min) comprised of air with P_{CO_2} = 0.3 atm, H_2 with P_{H_2O} = 0.3 atm and P_{CO_2} = 0.3 atm, and H_2 with P_{H_2O} = 0.3 atm (dictated by air/CO_2, H_2/CO_2, and H_2, respectively). After the completion of the experiments, $LiAlO_2$ powder was washed with a mixture solution of glacial acetic acid (>99.5%, Sigma-Aldrich) and acetic anhydride (>99%, Sigma-Aldrich) to dissolve the remaining carbonate electrolyte. Subsequently, $LiAlO_2$ powder was filtered through filter paper (0.1 μm diameter pore) and then dried at 120 °C for 4 h for characterization.

Characterization. XRD patterns were obtained using a Bruker D8 Advance system with Cu Kα radiation (λ = 1.5406 Å) to identify the phase structure of $LiAlO_2$ samples. The data were acquired over an angular range of $10° < 2\theta < 70°$ with a scan step of 0.02°. Surface morphologies were obtained using an FEI Quanta 250 FEG high-resolution scanning electron microscope with a field emission source and images using an Everhart-Thornley SE (secondary electron) detector with an electron accelerating voltage of 10 kV and a sample height of 10 mm. To investigate the morphologies and structures of the $LiAlO_2$ samples, TEM measurements were performed using a JEOL JEM-2010 FasTEM with an accelerating voltage of 200 kV. Focused ion beam (FEI Strata 400s Dual Beam FIB) was applied to obtain samples for TEM analysis. A platinum layer was initially deposited on the $LiAlO_2$ sample surface by electron beam to protect the samples from further ion beam damage.

First-Principles Calculations. Electronic structure DFT calculations were performed to study the role of surface energies on the crystal shape, and the possible phase transformation empirically observed in $LiAlO_2$ under different conditions. DFT calculations were performed using the Vienna Ab Initio Simulation Package (VASP) employing the Perdew–Burke–Ernzerhof exchange-correlation functional and the projector-augmented wave methodology. The basis set includes all the plane waves with kinetic energies up to 600 eV.

Starting from the structural parameters obtained from Rietveld refinement results on XRD analysis for both α- and γ-$LiAlO_2$, the bulk structures corresponding to the two allotropic forms of rhombohedral α-$LiAlO_2$ and tetragonal γ-$LiAlO_2$, were first optimized using DFT. The optimized parameters were as follows: α-$LiAlO_2$ ($R\bar{3}m$; a = 2.82 Å and c = 14.39 Å) and γ-$LiAlO_2$ ($P4_12_12$; a = 5.21 Å and c = 6.29 Å). With use of these DFT relaxed bulk structures, slabs with orientations (001), (012), (104), and (110) for the α-$LiAlO_2$ and (001), (100), (110), (102), and (101) for the γ-$LiAlO_2$ phase were constructed with a vacuum layer of 12 Å. The choice of the surfaces considered in each phase was guided from the peaks observed in the XRD pattern, the scanning electron microscopy (SEM) and high-resolution TEM (HRTEM) observations made in the present work, past works on structurally similar $LiMO_2$ (M: Ni, Mn, Co) systems,[24,25] and the expected low energy associated with stoichiometry surfaces with low Miller index. In particular, besides the low Miller index surfaces, (104) for α-$LiAlO_2$ and (102) for γ-$LiAlO_2$ were chosen because of XRD and HRTEM analysis. Furthermore, all of the surface slabs considered were stoichiometric. While in most cases the stoichiometric surfaces could only be terminated in a unique manner, there were a few cases wherein the surface termination had multiple possibilities. Such cases will be discussed in detail later. All atoms were relaxed until the components of forces were smaller than 0.01 and 0.05 eV/Å in the case of bulk and slab geometries, respectively.

The free surface energy (σ) was computed using the formulation

$$\sigma = \frac{1}{2A}[E_{slab} - n\varepsilon_b] \quad (1)$$

where E_{slab} is the energy of the stoichiometric slab, ε_b is the per formula-unit energy of the bulk $LiAlO_2$, and n denotes the number of formula units of $LiAlO_2$. Convergence studies of surface energies with respect to number of $LiAlO_2$ layers were also performed, details of which have been provided in Tables S1 and S2, Supporting Information.

To capture the effect of various conditions studied empirically, relevant low-energy surfaces were further passivated with different concentrations of H atoms. Initial structures in such cases were built by placing H atoms (in form of a monolayer) directly on top or below the O atoms at a distance of roughly 1 Å. Furthermore, the concentration of H atoms was computed in terms of the percentage of surface O atoms that were passivated by H atoms. The surface energy of

DOI: 10.1021/acs.jpcc.8b09716
J. Phys. Chem. C 2018, 122, 28797–28804

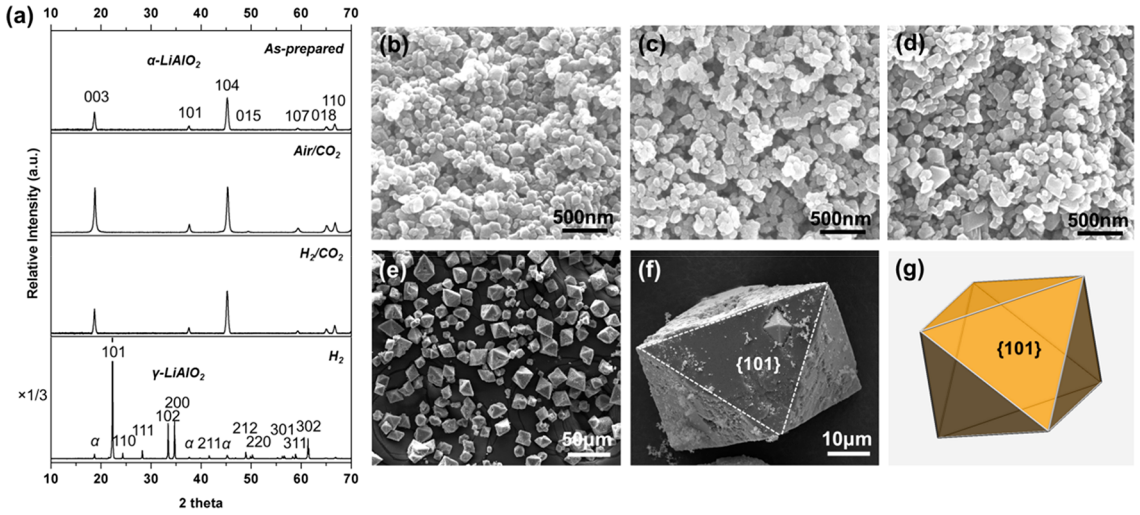

Figure 1. XRD patterns (a) and SEM images (b–f) of $LiAlO_2$ under different chemical environments; (b) as-prepared, (c) air/CO_2, (d) H_2/CO_2, and (e,f) H_2. (g) Schematic illustration of $LiAlO_2$ with the {101} surface planes. In (a), the XRD patterns of rhombohedra α-$LiAlO_2$ (JCPDS No. 74-2232) and tetragonal γ-$LiAlO_2$ (JCPDS No. 73-1338) phases are indexed. For clarity, the XRD intensity of the sample exposure to H_2 has been reduced to one-third.

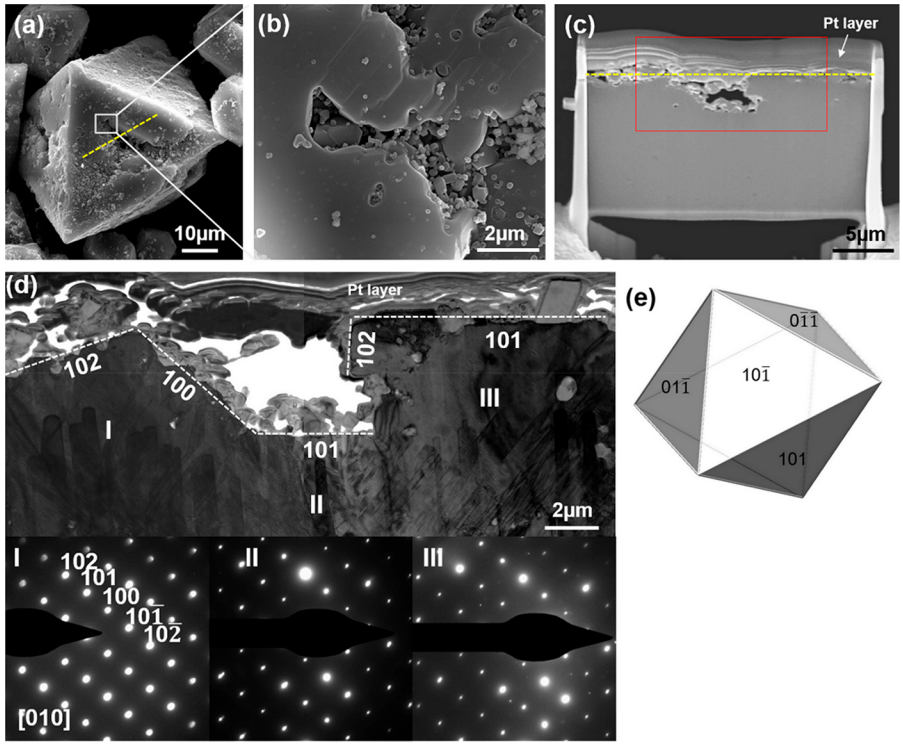

Figure 2. H_2-exposed $LiAlO_2$ as observed by SEM (a and b). FIB image is shown in (c) after the sample is cut along the dotted line in (a). (d) TEM image and SAED showing γ-$LiAlO_2$ terminated with {101} surfaces. Corresponding schematic illustration of γ-$LiAlO_2$ with the {101} surface planes is shown in (e).

a H-passivated surface as a function of μ_H was computed using the formulation

$$\sigma = \frac{1}{2A}\left[E_{slab} - n\varepsilon_b - n_H\left(\mu_H - \frac{1}{2}\mu_{H_2}\right)\right] \quad (2)$$

where n_H is the number of H atoms, μ_{H_2} is the DFT computed potential energy of H_2 molecule, and μ_H is the variable chemical potential of H. The remaining terms are as described earlier.

RESULTS AND DISCUSSION

Structural and Morphological Transformations. To investigate the structural and morphological stability of $LiAlO_2$ under different environments, we expose the prepared $LiAlO_2$ samples to air/CO_2, H_2/CO_2, and H_2 atmospheres. The crystallinity and morphology of the products were studied using XRD and SEM, respectively. The top panel in Figure 1a shows the XRD patterns of the as-prepared a-$LiAlO_2$. Two dominant diffraction peaks at 18.7 and 45.2 correspond to the (003) and (104) planes of rhombohedra α-$LiAlO_2$ phase.[26]

DOI: 10.1021/acs.jpcc.8b09716
J. Phys. Chem. C 2018, 122, 28797–28804

The high-resolution SEM images (Figure 1b) show that the as-prepared pure α-$LiAlO_2$ powders contained agglomerated nanospherical particles. Even for the products collected from exposed air/CO_2 and H_2/CO_2 atmospheres, the structure and morphology of α-$LiAlO_2$ remained unchanged (Figure 1a,c,d). This is in agreement with reports that show oxidizing atmospheres with a sufficient amount of CO_2 gas prevent dissociation of $LiAlO_2$.[27] However, under H-rich environment and in the absence of CO_2 gas, the peak intensities of α-$LiAlO_2$ were found to significantly decrease, while the γ-$LiAlO_2$ phase[28] with distinctly strong peaks for (101), (102), and (200) planes were detected (see bottom panel in Figure 1a). Furthermore, the γ-$LiAlO_2$ particles were found to crystallize with a clean octahedral morphology (see Figure 1e–g).

The octahedral $LiAlO_2$ particle obtained after exposure to H_2 atmosphere is cut with a FIB to closely examine its cross section (Figure 2a,c). The dotted yellow lines in Figure 2a,c correspond to the same position in the $LiAlO_2$ particle. The TEM results and corresponding selected area electron diffraction (SAED) patterns taken from three regions indicated by I, II, and III (Figure 2d) suggest that the octahedral particle has a single γ-$LiAlO_2$ crystal with [010] zone axis. Furthermore, the diffraction patterns indicate that the particle surface is predominately terminated by (101), (100), and (102) planes, which is in good agreement with the XRD results shown in Figure 1a. The TEM (Figure 2d) and SEM (Figure 2b) images also show the presence of relatively smaller particles forming rough surface regions. On the basis of these images, it appears that these smaller particles could grow and coalesce together to result in near-perfect octahedral geometry terminated by {101} surfaces, as illustrated in Figure 2e. This result is also in concordance with XRD results (Figure 1a) of the strongest peak for the (101) plane and relatively weak peaks for (102) and (100) planes.

The SEM images (Figure 3) also prove that γ-$LiAlO_2$ particles exhibit a truncated octahedral morphology with {101} and {110} planes. The magnified micrographs (Figure 3a_3, b_3, and c_3) reveal that the {101} surfaces are quite smooth,

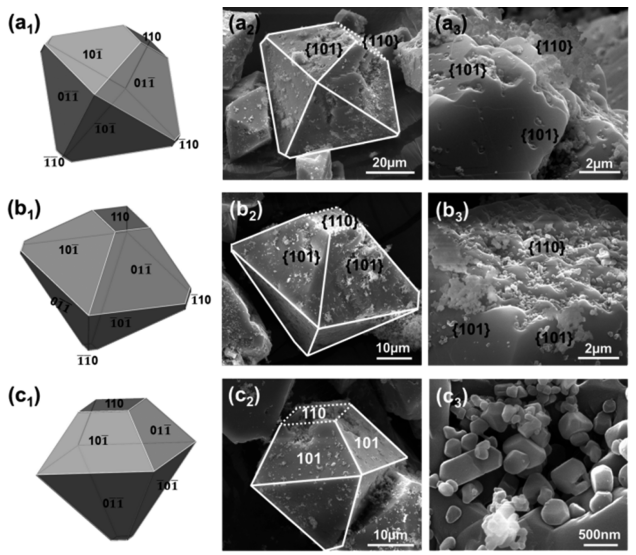

Figure 3. Schematic illustration (a_1–c_1) and SEM images (a_2–c_2) of γ-$LiAlO_2$ with the {101} and {110} surface planes. Magnified SEM images (a_3–c_3) show truncated octahedral crystals with rough {110} surface planes.

whereas the {110} surfaces are rough because of the presence of relatively smaller particles. This further suggests that most likely {110} surfaces are outgrown to form large γ-$LiAlO_2$ particles with a near-perfect octahedral morphology and {101} terminations. We note that crystal facets evolve to have the lowest surface energy during the crystal growth process while the higher energy facets tend to disappear.[29,30] Therefore, first-principles theoretical studies can help us understand these observations of octahedral-shaped particles and formation of γ-$LiAlO_2$ phase upon exposure to H_2 gas.

Morphology of γ-$LiAlO_2$ from DFT Computations. To understand the aforementioned empirical observations of phase transformation and crystal growth in $LiAlO_2$, first-principles DFT calculations were performed. Because empirically much of the structural and morphological changes were observed under varying H_2 atmospheres, we studied only the effect of H concentration by modeling both free and H-passivated α- and γ-$LiAlO_2$ surfaces. The free surface energies for the low Miller index surfaces of γ-$LiAlO_2$ under stoichiometric orientations are summarized in Table 1. We

Table 1. DFT Computed Free Surface Energies (J/m^2) of Different Stoichiometric Orientations of γ-$LiAlO_2$

facet	γ-$LiAlO_2$
(100)	1.279 J/m^2
(110)	1.502 J/m^2
(101)	1.551 J/m^2
(001)	1.568 J/m^2
(102)	1.692 J/m^2

note that stoichiometric (100), (001), and (102) slabs can only be terminated in a unique manner with an equal number of broken Li–O and Al–O bonds, while the (101) and (110) surfaces have three possible terminations with varying ratios of broken Li–O and Al–O bonds. For the latter cases, all three combinations were studied and the terminations with a smaller ratio of broken Al–O/Li–O bonds were found to have lower surface energies, suggesting that the Al–O bond breakage has higher energy cost. Thus, for the case of (101) and (110) only the lowest energy terminations have been reported in Table 1. Overall, the (100) surface was found to have the lowest free surface energy, which is in agreement with the aforementioned XRD and TEM analysis on γ-$LiAlO_2$ particles (under H_2-rich conditions). However, TEM analysis revealed (101), (110), and (102) surfaces to be more dominant, with {101} being the most prevailing surface plane. This seems to be in contradiction with the DFT predictions of these surfaces having relatively higher free surface energies because of the higher number of broken Al–O and Li–O bonds, as captured in Figure 4a,c. However, we note that the experimental conditions correspond to H-rich conditions, and thus there is a strong possibility that such "dangling" Al–O or Li–O bonds are passivated with H, thereby leading to reduced (101), (110), and (102) surface energies. Bader charge analysis[31] on different surfaces of γ-$LiAlO_2$ also suggests the occurrence of Al in reduced oxidation state at the surface as compared to that in the bulk (Table S3).

To test this hypothesis, we studied the surface energetics of the γ-$LiAlO_2$ as a function of H chemical potential ($\Delta\mu$(H)), with the results presented in Figure 5 and Figures S1–S5. For (101) and (110) surfaces that display many possible terminations, only the cases with lowest free surface energy,

DOI: 10.1021/acs.jpcc.8b09716
J. Phys. Chem. C 2018, 122, 28797–28804

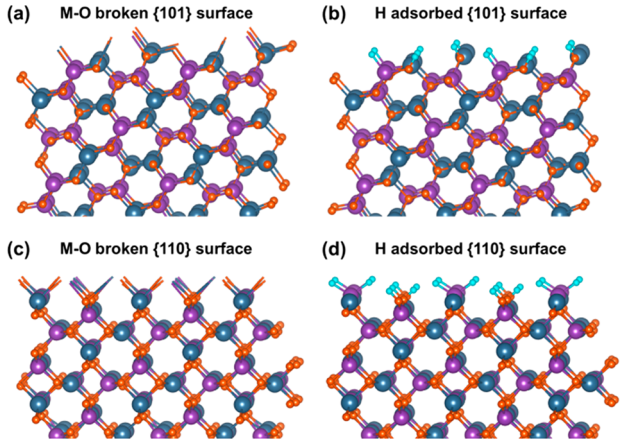

Figure 4. Surface geometries of the H-free (a, c) and the H-adsorbed (b, d) (101) and (110) surfaces, respectively. Blue, Li; purple, Al; orange, O; cyan, H.

that is, the surface terminations reported in Table 1, were considered for H-passivation studies. Furthermore, it should be noted that, in Figure 5, higher H chemical potential corresponds to H-rich conditions, with chemical potential of H_2 gas taken as reference. As can be seen from eq 2, the slope in Figure 5 is dependent on the number of passivating H atoms. Thus, for the case with zero passivating H atoms (or a free surface), the surface energy is independent of $\Delta\mu$(H). Clearly, (001) and (100) facets do not prefer H passivation as their free surface energies are lower than the respective H-passivated surfaces, suggesting that these surfaces do not form stronger bonds with H atoms. In contrast, the (110) and (102) facets with partial H-passivation (0.5H) have lower surface energies in H-rich conditions, indicating that these surfaces become stabilized at higher H partial pressure. More importantly, the (101) facet with 0.66H (66% of H on the surface) is found to have the lowest surface energy for almost the entire range of $\Delta\mu$(H) considered here.

We can recast the surface energy data in Figure 5 to find lowest energy facets of γ-$LiAlO_2$ as a function of $\Delta\mu$(H) and construct Figure 6a. In H-poor conditions (i.e., $\Delta\mu$(H) < 1.5 eV), the (100) facet has the lowest surface energy, followed by (101), (110), (001), and (102) surfaces. However, with an increase in H chemical potential, the surface energy of (101) facet considerably reduces relative to the others. Thus, under H-rich conditions, the surface energetics follow the trend (101) < (110) < (100) < (001) ~ (102) as captured in Figure 6a. A closer inspection of the relaxed structures revealed an interesting effect of H-passivation. Although initially the H atoms were placed near the O atoms to assist O−H bond formation, during the (101) slab relaxation the H atoms moved closer to the Al atoms to form Al−O bonds (see Figure 4c). More importantly, such behavior was absent in other surfaces considered. Thus, the formation of Al−H bond (or passivation of broken Al−O bonds) could be critical to lower the {101} surface energy, and perhaps lead to stabilization of the γ-$LiAlO_2$ phase under H-rich conditions, as corroborated by the XRD, SEM, and TEM observations presented earlier.

The DFT computed surface energy data of γ-$LiAlO_2$ could further be used to estimate the plausible morphology of γ-$LiAlO_2$ particles under varying H environment, and compared with the previously discussed SEM and TEM analysis. Thus, in Figure 6b we present the DFT predicted equilibrium particle shape of γ-$LiAlO_2$ at five different values of H chemical potential. The particle shapes are obtained using Wulff construction, which is based on minimization of total surface energy for a given volume of material.[32] As evident for Figure 6b, under H-poor conditions, the {100} surfaces have the lowest surface energy and accordingly the largest face area. However, with increasing H potential, the {101} surface energy reduces, and the {100} surfaces are superseded by {101} surfaces. Thus, DFT predicts a truncated octahedral morphology with exposed {101} and {110} surfaces at $\Delta\mu$(H) = −0.4 eV and finally a near-perfect octahedral shape with {101} surfaces at $\Delta\mu$(H) ~ 0 eV, both of which are in excellent

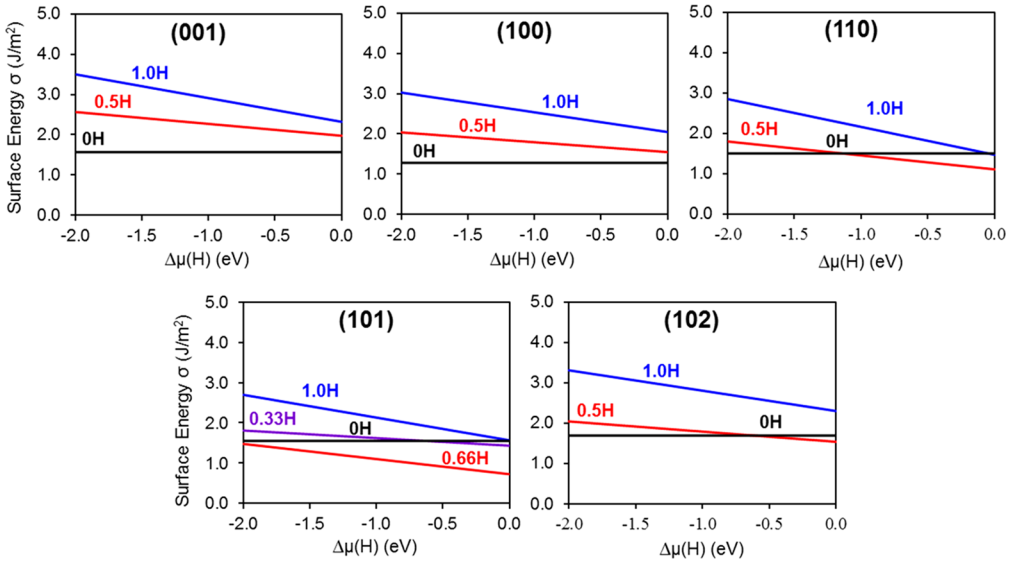

Figure 5. DFT computed surface energies of (001), (100), (110), (101), and (102) facets of γ-$LiAlO_2$ as functions of H chemical potential ($\Delta\mu$(H)) using eq 2. While 0H represents the H-free surface, 0.33H, 0.5H, 0.66H, and 1.0H correspond to 33%, 50%, 66%, and 100% surface coverage with H, respectively.

DOI: 10.1021/acs.jpcc.8b09716
J. Phys. Chem. C 2018, 122, 28797−28804

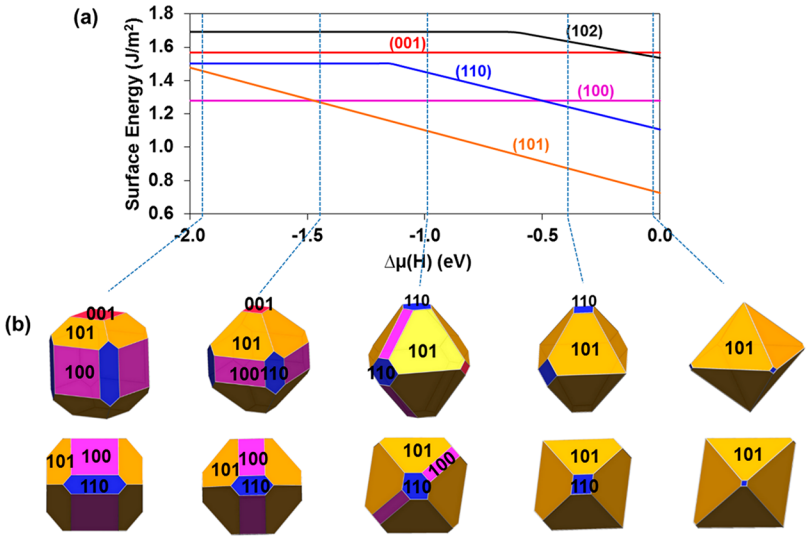

Figure 6. (a) DFT computed lowest value of surface energies for (100), (001), (110), (101), and (102) facets of γ-$LiAlO_2$ as a function of $\Delta\mu$(H). (b) Side (up) and top (down) view of crystal morphologies of γ-$LiAlO_2$ particle as obtained from Wulff construction at five different values of $\Delta\mu$(H).

agreement with the TEM and SEM observations presented earlier.

First-Principles Calculation: Phase Transformation of $LiAlO_2$. To further explore the potential role of H-passivation in transformation of rhombohedral α-$LiAlO_2$ to tetragonal γ-$LiAlO_2$ phase, we next performed similar DFT computations on α-$LiAlO_2$ surfaces. The free surface energies of four stoichiometric α-$LiAlO_2$ surfaces considered in this work are presented in Table 2. The relative ordering of surface energies

Table 2. DFT Computed Surface Energies (J/m^2) of α-$LiAlO_2$, $LiMO_2$ (M: $Ni_{1/3}$, $Mn_{1/3}$, $Co_{1/3}$),[24] and $LiNiO_2$[25] Systems

facet	α-$LiAlO_2$	$LiMO_2$	$LiNiO_2$
(104)	0.901 J/m^2	0.76 J/m^2	0.53 J/m^2
(001)	1.126 J/m^2	0.89 J/m^2	0.71 J/m^2
(110)	1.951 J/m^2	1.32 J/m^2	1.22 J/m^2
(012)	2.018 J/m^2	1.97 J/m^2	0.99 J/m^2

match well with past works on $LiMO_2$ (M: Ni, Mn, Co)[24] and $LiNiO_2$[25] systems which are chemically and structurally (rhombohedral phase) similar to α-$LiAlO_2$ with the exception of ordering of (110) and (012) surface energies in $LiNiO_2$. Similar to the case of γ-$LiAlO_2$, we note that (104) and (110) surfaces of α-$LiAlO_2$ have a unique termination possibility, while (001) and (012) surfaces can be cleaved in many possible ways. However, inspired from past works[33] and our work on γ-$LiAlO_2$, we report here energies for only the cases with the least number of broken Al−O bonds, while maintaining the stoichiometry of the slab. Among all the surfaces considered, the (104) facet has the lowest surface energy because of the small number of broken Li−O and Al−O bonds (see Figure 7). The (001) surface follows next. These DFT predictions are in good agreement with the XRD pattern in Figure 1a, wherein the (001) and (104) planes were indexed in high intensity.

Figure 8 presents the effect of H passivation on α-$LiAlO_2$ surfaces. As evident from the figure, for all cases H passivation results in higher surface energies than their respective free surface counterparts over the entire range of $\Delta\mu$(H). This suggests that H passivation is energetically unfavorable in the case of α-$LiAlO_2$. Therefore, this observation of increase in the

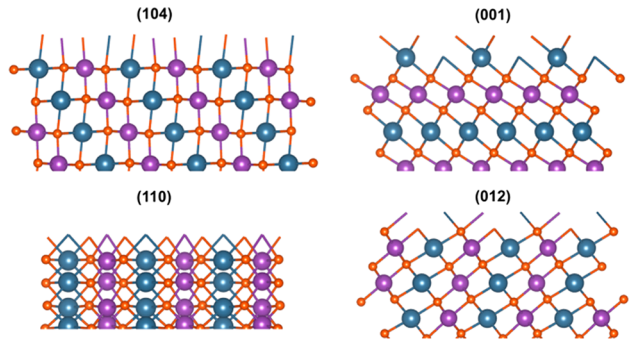

Figure 7. Surface geometries of the H-free (104), (001), (110), and (012) surfaces of α-$LiAlO_2$. Blue, Li; purple, Al; orange, O.

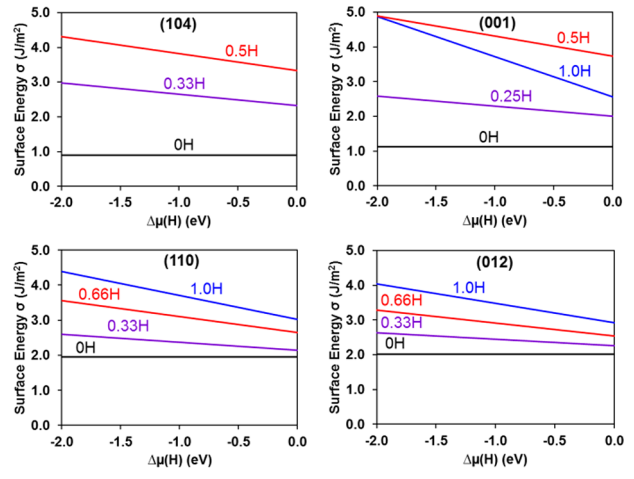

Figure 8. Surface energies of the H-free and the H-adsorbed (104), (001), (110), and (012) surfaces of α-$LiAlO_2$ as a function of hydrogen chemical potential. 0H represents the H-free on the surface and 0.25H, 0.33H, 0.5H, 0.66H, and 1.0H is 25%, 33%, 50%, 66%, and 100% of H-adsorption on the surfaces, respectively.

DOI: 10.1021/acs.jpcc.8b09716
J. Phys. Chem. C 2018, 122, 28797−28804

energy of the α-$LiAlO_2$ surface under H-rich conditions combined with the previous results of stabilization of γ-$LiAlO_2$ (101) surfaces could be the driving force for the formation of γ-$LiAlO_2$ crystals.

Thus, putting together the empirical and the theoretical analysis, a schematic of the structural and morphological changes in $LiAlO_2$ under H-rich atmospheres is presented in Figure 9. The as-prepared $LiAlO_2$ powder consisted of small

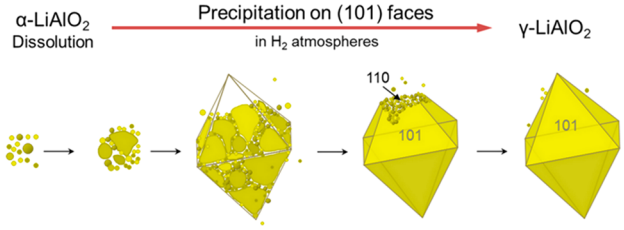

Figure 9. Schematic representation of proposed morphological and phase transformation processes.

particles in the rhombohedral α-$LiAlO_2$ phase, as suggested clearly by the XRD analysis. However, upon exposure to reducing atmospheres, that is, H_2 gas, a phase transformation to the γ-$LiAlO_2$ phase along with a distinct morphological preference to formation of {101}-terminated octahedral crystallites was observed. Some crystallites with truncated octahedral morphology (preferentially along (110)) were also observed, most likely representing cases with incomplete particle growth. A combination of XRD, SEM, and TEM analysis was adopted to deduce these structural and morphological findings. However, to develop a fundamental understanding of the observed transformations, we performed first-principles DFT calculations of various α-$LiAlO_2$ and γ-$LiAlO_2$ surfaces under H-rich and H-poor conditions. Although the DFT models are much simpler than the synthesized empirical $LiAlO_2$ system, the computations clearly revealed that the {101} and {110} surfaces of γ-$LiAlO_2$ are energetically stabilized under H-rich conditions, with {101} being lowest in energy. Interestingly, an opposite trend of the increase in energy of α-$LiAlO_2$ surface upon H passivation was also found using DFT computations. Thus, the DFT surface energy predictions are in excellent agreement with empirical observations confirmed using XRD, SEM, and TEM analysis and provide a plausible explanation of the increase in the volume fraction of γ-$LiAlO_2$ under H-rich conditions in terms of thermodynamic considerations of stabilization of γ-$LiAlO_2$ surfaces as opposed to that of α-$LiAlO_2$.

CONCLUSIONS

Layered α-$LiAlO_2$ is commonly used as an electrolyte matrix in molten carbonate fuel cells. Under a H_2-rich MCFC environment, α-$LiAlO_2$ undergoes a phase transformation (accompanied by morphological changes) detrimental to the efficient working of fuel cells. Using XRD, SEM, and TEM analysis, we confirm the α-$LiAlO_2$ to γ-$LiAlO_2$ transformation and study the accompanying crystal morphology. We find that, under H-rich conditions, the morphology of the $LiAlO_2$ particles is a perfect octahedron and most of the rhombohedral α-$LiAlO_2$ phase transforms to the tetragonal γ-$LiAlO_2$ phase. TEM analysis of the FIB-lifted samples revealed that the octahedral morphology has single γ-$LiAlO_2$ crystal terminated by {101} surfaces. Furthermore, the electron microscopy analysis of truncated octahedral crystals suggested growth of {110} surfaces into {101}, resulting in perfect octahedral γ-$LiAlO_2$ crystals.

To understand these experimental observations, first-principles DFT computations were performed to examine surface energetics of both α-$LiAlO_2$ and γ-$LiAlO_2$ phases with and without H passivation. The DFT computations not only revealed the low-energy surfaces for each phase, in-line with the X-ray diffraction (XRD) peak analysis, but also helped to predict the $LiAlO_2$ crystallite shape using Wulff construction. In agreement with empirical observations, the DFT results suggest substantial reduction in {101} surface energy of γ-$LiAlO_2$ under H-rich conditions, leading to near-perfect octahedral geometry of $LiAlO_2$ particles. The DFT predicted surface energy ordering of {110} having higher energy than {101} surfaces in γ-$LiAlO_2$ also provides a possible explanation of the observed truncated octahedral particles. Furthermore, the opposite trend of increase and decrease in the surface energy of α-$LiAlO_2$ and γ-$LiAlO_2$, respectively, under H-rich conditions could be a plausible driving force for α-$LiAlO_2$ to γ-$LiAlO_2$ phase transformation. Structurally, the formation of Al−H bonds on {101} surfaces of γ-$LiAlO_2$ were found to be responsible for lowered surface energies. These results provide a fundamental understanding of the morphology and phase of matrix materials and a new approach to examine and select layered and other matrix materials.

ASSOCIATED CONTENT

Supporting Information

The Supporting Information is available free of charge on the ACS Publications website at DOI: 10.1021/acs.jpcc.8b09716.

Relaxed structures for H-free and H-passivated γ-$LiAlO_2$ slabs with varying H concentrations and convergence of surface energies for α- and γ-$LiAlO_2$ slabs (PDF)

AUTHOR INFORMATION

Corresponding Author

*E-mail: prabhakar.singh@uconn.edu.

ORCID

Su Jeong Heo: 0000-0002-7933-9714
Rohit Batra: 0000-0002-1098-7035
Rampi Ramprasad: 0000-0003-4630-1565
Prabhakar Singh: 0000-0002-5000-4902

Author Contributions

The manuscript was written through contributions of all authors. All authors have given approval to the final version of the manuscript.

Notes

The authors declare no competing financial interest.

ACKNOWLEDGMENTS

Authors acknowledge financial support from the U.S. Department of Energy under Contract DE-EE0006606. The authors gratefully acknowledge Dr. Chao-yi Yuh and Dr. Abdelkader Hilmi (FuelCell Energy Inc.) for valuable discussions and technical support. The Center for Clean Energy Engineering at the University of Connecticut is acknowledged for providing laboratory support and the use of its characterization facility. We also appreciate the assistance of Dr. Roger Ristau and Dr. Lichun Zhang of IMS at UConn for the FIB cut and TEM images.

DOI: 10.1021/acs.jpcc.8b09716
J. Phys. Chem. C 2018, 122, 28797−28804

REFERENCES

(1) Fang, Z. K.; Zhu, Y. R.; Yi, T. F.; Xie, Y. Li4Ti5O12-LiAlO2 Composite as High Performance Anode Material for Lithium-Ion Battery. *ACS Sustainable Chem. Eng.* **2016**, *4*, 1994−2003.

(2) Wiedemann, D.; Nakhal, S.; Rahn, J.; Witt, E.; Islam, M. M.; Zander, S.; Heitjans, P.; Schmidt, H.; Bredow, T.; Wilkening, M.; Lerch, M. Unravelling Ultraslow Lithium-Ion Diffusion in γ-LiAlO2: Experiments with Tracers, Neutrons, and Charge Carriers. *Chem. Mater.* **2016**, *28*, 915−924.

(3) Baron, R.; Wejrzanowski, T.; Milewski, J.; Szablowski, L.; Szczesniak, A.; Fung, K. Z. Manufacturing of γ-LiAlO2Matrix for Molten Carbonate Fuel Cell by High-Energy Milling. *Int. J. Hydrogen Energy* **2018**, *43*, 6696−6700.

(4) Gao, L.; Selman, J. R.; Nash, P. Wetting of Porous α-LiAlO2 by Molten Carbonate. *J. Electrochem. Soc.* **2018**, *165*, F324−F333.

(5) Lan, R.; Tao, S. A Simple High-Performance Matrix-Free Biomass Molten Carbonate Fuel Cell without CO2 Recirculation. *Sci. Adv.* **2016**, *2*, No. e1600772.

(6) Tomimatsu, N.; Ohzu, H.; Akasaka, Y.; Nakagawa, K. Phase Stability of LiAlO2 in Molten Carbonate. *J. Electrochem. Soc.* **1997**, *144*, 4182−4186.

(7) Heo, S. J.; Hu, B.; Uddin, M. A.; Aphale, A.; Hilmi, A.; Yuh, C. Y.; Surendranath, A.; Singh, P. Role of Exposure Atmospheres on Particle Coarsening and Phase Transformation of LiAlO2. *J. Electrochem. Soc.* **2017**, *164*, H5086−H5092.

(8) Takizawa, K.; Hagiwara, A. The Transformation of LiAlO2 Crystal Structure in Molten Li/K Carbonate. *J. Power Sources* **2002**, *109*, 127−135.

(9) Finn, P. A. The Effects of Different Environments on the Thermal Stability of Powdered Samples of LiAlO2. *J. Electrochem. Soc.* **1980**, *127*, 236−238.

(10) Terada, S.; Nagashima, I.; Higaki, K.; Ito, Y. Stability of LiAlO2 as electrolyte matrix for molten carbonate fuel cells. *J. Power Sources* **1998**, *75*, 223−229.

(11) Choi, H. J.; Lee, J. J.; Hyun, S. H.; Lim, H. C. Phase and Microstructural Stability of Electrolyte Matrix Materials for Molten Carbonate Fuel Cells. *Fuel Cells* **2010**, *10*, 613−618.

(12) Marezio, M.; Remeika, J. P. High-Pressure Synthesis and Crystal Structure of α-LiAlO2. *J. Chem. Phys.* **1966**, *44*, 3143−3144.

(13) Kim, H. S.; Oh, Y.; Kang, K. H.; Kim, J. H.; Kim, J.; Yoon, C. S. Characterization of Sputter-Deposited LiCoO2 Thin Film Grown on NASICON-type Electrolyte for Application in All-Solid-State Rechargeable Lithium Battery. *ACS Appl. Mater. Interfaces* **2017**, *9*, 16063−16070.

(14) Chen, H.; Wu, L.; Zhang, L.; Zhu, Y.; Grey, C. P. LiCoO2 Concaved Cuboctahedrons from Symmetry-Controlled Topological Reactions. *J. Am. Chem. Soc.* **2011**, *133*, 262−270.

(15) Yoon, C. S.; Choi, M. J.; Jun, D. W.; Zhang, Q.; Kaghazchi, P.; Kim, K. H.; Sun, Y. K. Cation Ordering of Zr-Doped LiNiO2 Cathode for Lithium-Ion Batteries. *Chem. Mater.* **2018**, *30*, 1808−1814.

(16) Abakumov, A. M.; Tsirlin, A. A.; Bakaimi, I.; Van Tendeloo, G. V.; Lappas, A. Multiple Twinning as a Structure Directing Mechanism in Layered Rock-Salt-Type Oxides: NaMnO2 Polymorphism, Redox Potentials, and Magnetism. *Chem. Mater.* **2014**, *26*, 3306−3315.

(17) Cho, E.; Seo, S.-W.; Min, K. Theoretical Prediction of Surface Stability and Morphology of LiNiO2 Cathode for Li Ion Batteries. *ACS Appl. Mater. Interfaces* **2017**, *9*, 33257−33266.

(18) Okubo, M.; Hosono, E.; Kim, J.; Enomoto, M.; Kojima, N.; Kudo, T.; Zhou, H.; Honma, I. Nanosize Effect on High-Rate Li-Ion Intercalation in LiCoO2 Electrode. *J. Am. Chem. Soc.* **2007**, *129*, 7444−7452.

(19) Islam, M. M.; Bredow, T. Interstitial lithium diffusion pathways in γ-LiAlO2: A computational study. *J. Phys. Chem. Lett.* **2015**, *6*, 4622−4626.

(20) Wang, W.; Yang, W.; Wang, H.; Li, G. Epitaxial Growth of GaN Films on Unconventional Oxide Substrates. *J. Mater. Chem. C* **2014**, *2*, 9342−9358.

(21) Nishikawa, M.; Baba, A.; Kawamura, Y. Tritium Inventory in a LiAlO2 Blanket. *J. Nucl. Mater.* **1997**, *246*, 1−8.

(22) Tsuchihira, H.; Oda, T.; Tanaka, S. Derivation of Potential Model for LiAlO2 by Simple and Effective Optimization of Model Parameters. *J. Nucl. Mater.* **2009**, *395*, 112−119.

(23) Heo, S. J.; Hu, B.; Manthina, V.; Hilmi, A.; Yuh, C. Y.; Surendranath, A.; Singh, P. Stability of Lithium Aluminate in Reducing and Oxidizing Atmospheres at 700°C. *Int. J. Hydrogen Energy* **2016**, *41*, 18884−18892.

(24) Garcia, J. C.; Bareno, J.; Yan, J.; Chen, G.; Hauser, A.; Croy, J. R.; Iddir, H. Surface Structure, Morphology, and Stability of Li(Ni1/3Mn1/3Co1/3)O2 Cathode Material. *J. Phys. Chem. C* **2017**, *121*, 8290−8299.

(25) Liang, C.; Longo, R. C.; Kong, F.; Zhang, C.; Nie, Y.; Zheng, Y.; Cho, K. Ab Initio Study on Surface Segregation and Anisotropy of Ni-Rich LiNi1−2yCoyMnyO2 (NCM) ($y \leq 0.1$) Cathodes. *ACS Appl. Mater. Interfaces* **2018**, *10*, 6673−6680.

(26) Li, L.; Chen, Z.; Zhang, Q.; Xu, M.; Zhou, X.; Zhu, H.; Zhang, K. A Hydrolysis-Hydrothermal Route for the Synthesis of Ultrathin LiAlO2-Inlaid LiNi0.5CO0.2Mn0.3O2 as a High-Performance Cathode Material for Lithium Ion Batteires. *J. Mater. Chem. A* **2015**, *3*, 894−904.

(27) Antolini, E. The Stability of LiAlO2 Powders and Electrolyte Matrices in Molten Carbonate Fuel Cell Environment. *Ceram. Int.* **2013**, *39*, 3463−3478.

(28) Marezio, M. The Crystal Structure and Anomalous Dispersion of γ-LiAlO2. *Acta Crystallogr.* **1965**, *19*, 396−400.

(29) Zhou, Z. Y.; Tian, N.; Li, J. T.; Broadwell, I.; Sun, S. G. Nanomaterials of High Surface Energy with Exceptional Properties in Catalysis and Energy Storage. *Chem. Soc. Rev.* **2011**, *40*, 4167−4185.

(30) Xu, G. L.; Wang, Q.; Fang, J. C.; Xu, Y. F.; Li, J. T.; Huang, L.; Sun, S. G. Turning the Structure and Property of Nanostructured Cathode Materials of Lithium Ion and Lithium Sulfur Batteries. *J. Mater. Chem. A* **2014**, *2*, 19941−19962.

(31) Yu, M.; Trinkle, D. R. Accurate and Efficient Algorithm for Bader Charge Integration. *J. Chem. Phys.* **2011**, *134*, 064111.

(32) Roosen, A. R.; McCormack, R. P.; Carter, W. C. Wulffman: A Tool for the Calculation and Display of Crystal Shapes. *Comput. Mater. Sci.* **1998**, *11*, 16−26.

(33) Andreu, N.; Baraille, I.; Martinez, H.; Dedryvere, R.; Loudet, M.; Gonbeau, D. New Investigations on the Surface Reactivity of Layered Lithium Oxides. *J. Phys. Chem. C* **2012**, *116*, 20332−20341.

DOI: 10.1021/acs.jpcc.8b09716
J. Phys. Chem. C 2018, 122, 28797−28804